





Integrated silicon carbide electro-optic modulator

Keith Powell^{1,2}, Liwei Li ¹, Amirhassan Shams-Ansari², Jianfu Wang¹, Debin Meng¹, Neil Sinclair^{2,3}, Jiangdong Deng ⁴, Marko Lončar ²✉ & Xiaoke Yi ¹✉

Owing to its attractive optical and electronic properties, silicon carbide is an emerging platform for integrated photonics. However an integral component of the platform is missing—an electro-optic modulator, a device which encodes electrical signals onto light. As a non-centrosymmetric crystal, silicon carbide exhibits the Pockels effect, yet a modulator has not been realized since the discovery of this effect more than three decades ago. Here we design, fabricate, and demonstrate a Pockels modulator in silicon carbide. Specifically, we realize a waveguide-integrated, small form-factor, gigahertz-bandwidth modulator that operates using complementary metal-oxide-semiconductor (CMOS)-level voltages on a thin film of silicon carbide on insulator. Our device is fabricated using a CMOS foundry compatible fabrication process and features no signal degradation, no presence of photorefractive effects, and stable operation at high optical intensities (913 kW/mm²), allowing for high optical signal-to-noise ratios for modern communications. Our work unites Pockels electro-optics with a CMOS foundry compatible platform in silicon carbide.

¹School of Electrical and Information Engineering, The University of Sydney, Sydney, NSW 2006, Australia. ²John A. Paulson School of Engineering and Applied Sciences, Harvard University, Cambridge, MA 02138, USA. ³Division of Physics, Mathematics and Astronomy, and Alliance for Quantum Technologies (AQT), California Institute of Technology, 1200 E. California Boulevard, Pasadena, CA 91125, USA. ⁴Center for Nanoscale Systems, Harvard University, Cambridge, MA 02138, USA. ✉email: loncar@seas.harvard.edu; xiaoke.yi@sydney.edu.au

Being a compelling semiconductor material for next-generation electronic devices¹ and a contender for realizing integration of electrically-driven quantum emitters², there is motivation to investigate silicon carbide (SiC) for monolithically integrated photonics^{2–6}. By taking advantage of the high refractive index (~ 2.57), wide band-gap, low thermo-optic coefficient⁷, high electron mobility, and thermal conductivity⁸ of SiC, high-density integrated photonic devices can be fabricated in this material with robust properties. Furthermore, this may be accomplished with low fabrication costs due to its compatibility with complementary metal-oxide-semiconductor (CMOS) foundry nanofabrication⁹, which also presents the opportunity for integration with electronics. The high optical damage threshold and bulk Young's modulus of 450 GPa add to the potential of SiC devices operating in harsh environments.

One critical component for SiC photonics remains outstanding, that is, to demonstrate an electro-optic (EO) modulator using the Pockels (or linear EO) effect. This effect, which exists in non-centrosymmetric crystals such as SiC, allows the refractive index to vary linearly and rapidly in proportion to an applied electric field. Consequently, Pockels-based modulators are exploited to achieve high data rates and microwave-conversion efficiencies without the addition of optical loss¹⁰ and are foundational to many applications¹¹. Despite the discovery of the Pockels effect in bulk cubic SiC (3C-SiC) more than three decades ago¹², an integrated electro-optic modulator has yet to be realized in SiC for a number of reasons including poor crystal quality and difficulty realizing low-loss waveguides^{13–16}. Although 3C-SiC can be grown directly onto a silicon substrate, it has been difficult to obtain high-quality thin films due to crystal defects associated with this approach^{7,17,18}. Wafer bonding techniques¹⁹ and annealing processes⁷ have been explored to address these problems. Yet, the former approach yielded multimode waveguides, while the latter resulted in a high (7 dB/cm) optical loss. These issues undermine a SiC Pockels modulator, specifically one that features single-mode waveguides for stable and high extinction-ratio ring modulators or quantum applications²⁰.

Here we design, fabricate and demonstrate a SiC EO modulator. Optical modulation is achieved by electrically driving a microring resonator based on sub-micron-wide 3C-SiC-on-insulator waveguides via the Pockels effect. A microring is chosen to enable a compact device footprint ($90 \mu\text{m}^2$) while maintaining high modulation performance at low voltage. The modulator is fabricated with a CMOS foundry compatible process and operates at a transmission rate of up to 15 Gbit/s using CMOS-level drive voltages. Importantly, we reduce the impact of polycrystal grains and waveguide surface roughness compared to previous work to demonstrate ~ 5.2 dB/cm optical loss using a single-mode waveguide. As a consequence of our work, we measure the Pockels coefficient (1.5 pm/V) of 3C-SiC at an infrared wavelength. Moreover, the modulator is able to operate continuously at high optical intensities of up to 913 kW/mm^2 without signal degradation or the presence of photorefractive, facilitating low-noise microwave and nonlinear photonics²¹ or potentially parametric frequency conversion of weak fields²².

Results

Design and fabrication. The fabrication of the integrated 3C-SiC modulator begins with a 530 nm-thick SiC layer with a low crystal defect density (see Methods) to reduce the scattering or absorption losses and increase EO interaction. Figure 1a shows an optical micrograph of a fabricated modulator capable of being driven by a CMOS digital-to-analog converter (DAC). The modulator consists of a pair of 3C-SiC vertical grating couplers (VGCs) as optical input and output ports, an optical waveguide

ring resonator with a loaded quality (Q_L) factor of 34,310 to balance modulation efficiency and bandwidth²³, and microwave stripline electrodes to deliver electrical signals. The waveguides and the VGCs are structured by electron beam lithography (EBL) (see Methods), in which a typical waveguide width of 800 nm is chosen to maintain single-mode operation with high optical mode confinement. The electrodes consist of a pair of ground electrodes placed next to the sides of the waveguide and a signal electrode above the waveguide (Fig. 1b). A 1 μm -thick top cladding SiO_2 layer is deposited to separate the electrode to the waveguide, which prevents optical loss due to mode interaction with the metal. Figure 1c shows a cross-sectional scanning electron micrograph (SEM) of the modulator to illustrate the geometries of the waveguide and electrodes. The electrode thickness (~ 500 nm) is chosen to reduce radio frequency (RF) loss due to the skin effect. As depicted in Fig. 1d, when a voltage is applied across the signal and ground electrodes, a vertical electric field is induced predominantly in the vertical direction overlapping with the optical mode to probe the Pockels effect. The ring cavity enables the phase change to be translated into an intensity-modulated output, where the resonant enhancement of the modulator allows for a small device footprint and low drive voltage operation. Figure 1e shows an SEM of our etched waveguide, which can achieve a root-mean-squared sidewall roughness $l < 2.4$ nm facilitating absorption-limited optical loss⁷. To quantify the optical loss, the optical spectrum of the microring resonator with critically coupled resonances operating at the telecommunication wavelengths (1569 nm–1600 nm) is measured to reveal single-mode operation (Fig. 1f) with a resonance linewidth of 35.4 pm (Fig. 1g). The obtained intrinsic Q (Q_i) is 89,281 corresponding to a linear propagation loss of ~ 5.2 dB/cm.

Modulator bandwidth and Pockels coefficient. To characterize the maximum operational bandwidth of our fabricated modulator, we examine the EO response at an optical input power of 6.8 mW (see Methods), which shows a 3 dB bandwidth of 7.1 GHz (Fig. 2a). The bandwidth is limited by the cavity photon lifetime of 28 ps, calculated based on the measured cavity linewidth (45 pm) that corresponds to the modulation bandwidth of around 5.7 GHz. The electrode circuit of the modulator has a much broader spectral response exceeding 30 GHz, as indicated in the inset of Fig. 2a. Therefore, higher bandwidths could be achieved by reducing the cavity Q factor, however, this will result in a lower modulation index with the same RF signal strength²³.

To determine the EO performance of the modulator, we use light at a wavelength of 1544.1 nm and drive the modulator with frequencies between 2.5 GHz and 17.5 GHz with a peak-to-peak drive voltage (V_{pp}) of 1 V (Methods) equivalent to an RF power of 1 mW. The generation of the pair of sidebands seen in the optical spectrum explicitly demonstrates the resultant intensity modulation (Fig. 2b). For increased frequency, a reduction in sideband power is observed, consistent with the roll-off induced by the resonant linewidth. Using the measured optical spectrum and determining the electric field strength inside the waveguide^{24,25}, we are able to determine the Pockels coefficient to be 1.5 pm/V (see Methods) which is similar to other CMOS foundry compatible EO materials including AlN (1 pm/V)^{25–27}. For a modulation frequency that is less than the resonator linewidth e.g. 2.5 GHz, the modulator can achieve an extinction ratio of 3 dB with $V_{pp} = 8$ V. The corresponding half-wave voltage-length product ($V_{\pi}L$) of SiC on insulator is calculated to be ~ 55 V \cdot cm (Methods). The combination of a low permittivity (~ 9.7)²⁸ and high refractive index²⁹ also allows for more efficient utilization of the linear EO effect in 3C-SiC over other materials, e.g. LiNbO_3 . With direct current (DC) voltages, a resonance shift

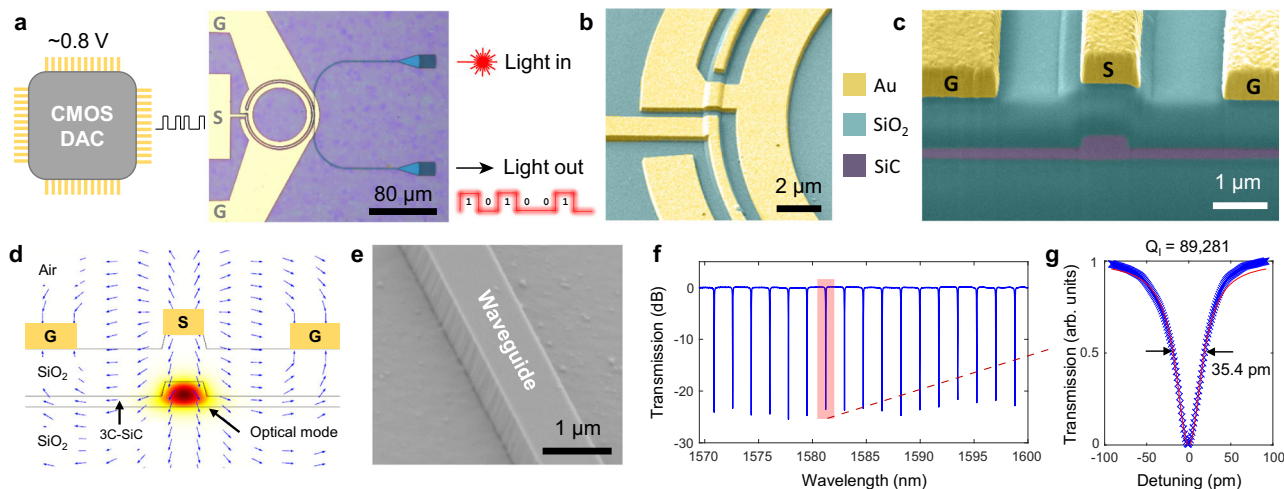


Fig. 1 Integrated Pockels modulator in SiC on insulator. **a** Overview of the fabricated ring modulator showing compatibility with CMOS voltages. **b** False color SEM of the microring waveguide and modulator electrodes. **c** False color SEM cross-section of the active region of the modulator. **d** Simulated static electric field and optical mode of the active region of the modulator. **e** SEM of an etched waveguide with the sidewall shown. **f** Measured optical spectrum of the SiC microring resonator after calibrating the optical loss from the VGCs. **g** Lorentz fit of the resonance line shape to determine the intrinsic optical quality factor (Q_i) (Cross: Measurement; Solid line: Lorentz fitting).

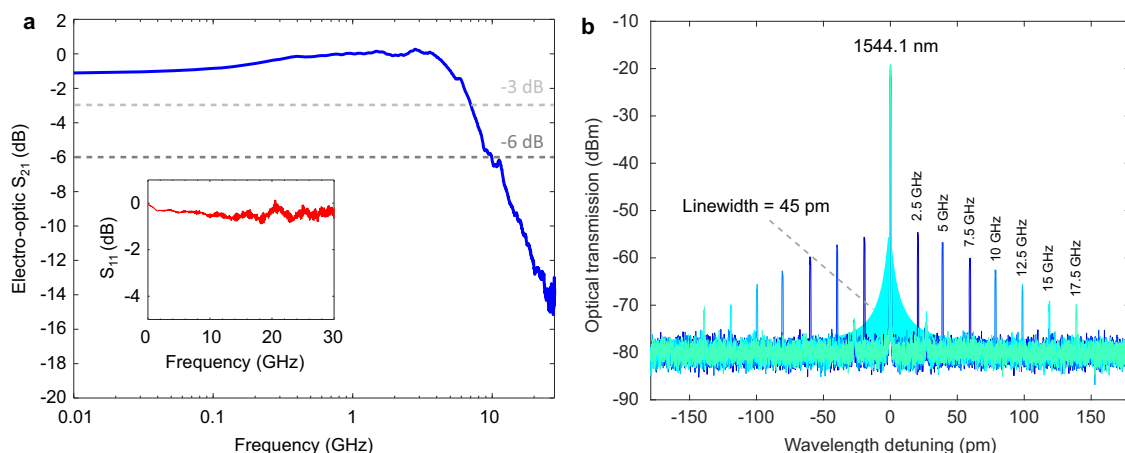


Fig. 2 Modulator bandwidth and EO characterization. **a** RF s -parameter characterization featuring a -3 dB and -6 dB bandwidths of 7.1 GHz and 9.9 GHz respectively. S_{21} transmission coefficient of the scattering matrix. Inset shows the S_{11} , reflection spectrum of the modulator. **b** Optical spectrum at the output of the modulator for various input RF frequencies. The measurement at 2.5 GHz which is within the resonator linewidth is used in the Pockels coefficient extraction.

of 0.11 pm/V (see Methods) is measured, which is lower than the measured RF shift likely due to shielding caused by trapped charges in the silicon-rich SiO_x layer²². This could be avoided by annealing or using higher purity thermal oxide.

Digital modulation performance at low drive voltages. To quantify the performance of our modulator for data transmission, we demonstrate low voltage operation with digital modulation (Methods). Using a non-return-to-zero (NRZ) pseudorandom bit sequence (PRBS) of 2^7 bits, we drive the modulator directly from a CMOS DAC operating with a V_{pp} ranging from 0.2 V to 2 V (Fig. 3a). Figure 3b shows the measured binary data over a period of 5 ns at a data rate of 5 Gb/s, with an optical input power of 6.8 mW using drive voltages of 2 V_{pp} and 1.2 V_{pp}, showing that the modulator correctly modulates the light intensity according to the applied digital sequence. Figure 3c depicts the modulator operating at low drive voltages, with an optical input power of 6.8 mW, across a range of modulation bandwidths with an eye Q_E factor >2.7 . When the drive voltage is reduced from $V_{pp} = 2$ V to

1.2 V, the modulator still maintains an open 5 Gb/s non-return-to-zero eye diagram, allowing for successful data transmission and detection. With $V_{pp} = 2$ V and an optical input power of 6.8 mW, the modulator supports bit rates up to 10 Gb/s, limited by the cavity photon lifetime bandwidth (5.7 GHz). The bit error ratio (BER)^{30,31} is obtained from the Q_E factor of the eye diagram measured by using a low-pass RF filter at the output of the photodetector for inter-symbol-interference reduction (see Methods). The measured eye diagram, Q_E , and the corresponding BER, at different drive voltages, are shown in Fig. 3d. We obtain a measured Q_E factor of 4.2 for a drive voltage of 0.8 V_{pp}, corresponding to a BER of 1.3×10^{-5} . This is lower than the forward error correction (FEC) limit^{32,33}.

High optical power operation. The ability for the modulator to operate at high optical powers without degrading the signal is important for enhancing signal-to-noise ratios in several applications^{21,22}. EO materials such as lithium niobate and barium titanate, suffer from signal distortion induced by photorefraction

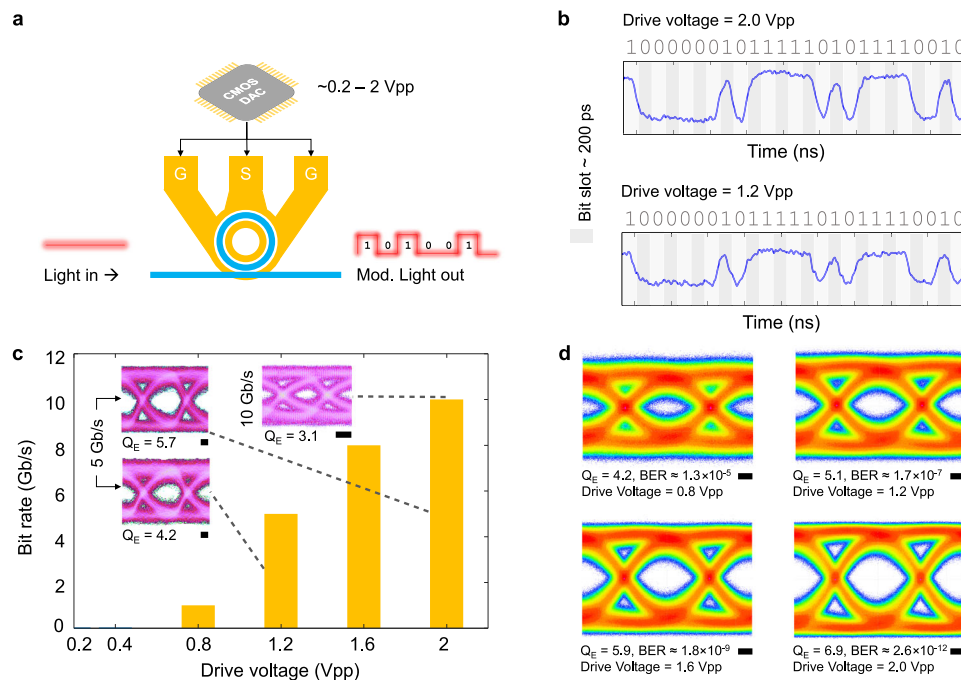


Fig. 3 Digital CMOS-level electro-optic modulation with non-return to zero (NRZ) pseudorandom bit sequence (PRBS) of 2^7 bits. **a** Setup configuration using a CMOS DAC to drive the ground-signal-ground (GSG) electrodes of the modulator. **b** Time-domain waveforms measured at the output of the modulator at 5 Gb/s for drive voltages of 2 Vpp and 1.2 Vpp, respectively. **c** Drive-voltage-dependent eye diagram quality factors (Q_E) for increasing bit rate. The bar plot shows the modulation bandwidth with $Q_E > 2.7$. The high-bandwidth photodiode is directly connected to a real-time oscilloscope for recording eye diagrams and Q_E without equalization. No low-pass RF filter is used in the measurement. **d** Measured eye diagrams and Q_E at 5 Gbit/s for different drive voltages. A low-pass RF filter is used at the output of the photodiode for inter-symbol-interference reduction. Eye diagrams and Q_E are measured via the oscilloscope without equalization. BER is estimated from the measured Q_E factor^{30,31}. Scale bars, 33 ps.

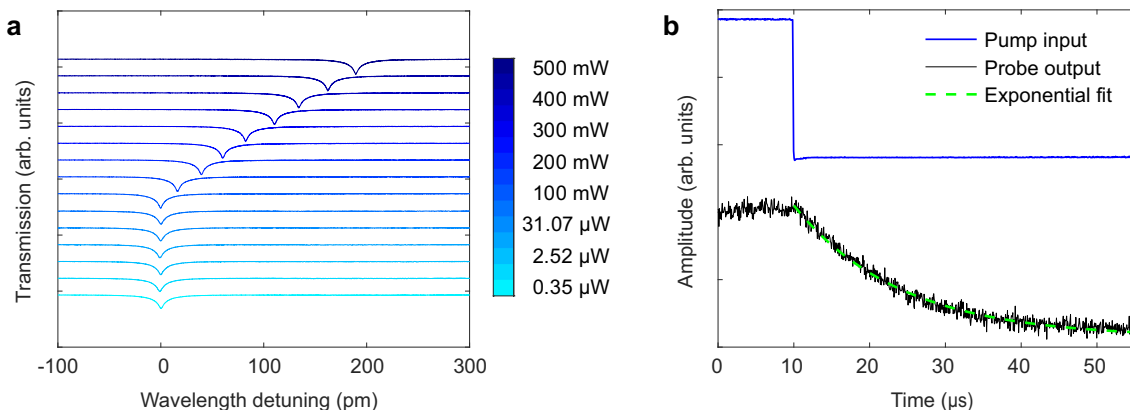


Fig. 4 Transmission spectra and relaxation of SiC resonator at high power. **a** Transmission spectra of the probed resonance at 1547 nm with a 1544 nm wavelength pump of varying powers (see colorbar) launching into the VGC to excite the resonator. **b** Step response showing the probe resonance after the pump beam (500 mW power) is switched off. The exponential decay is due to thermal relaxation.

that worsens with increasing optical powers^{34–36}, and is avoided by post-modulation amplification in applications. To evaluate the optical response of the modulator at high power, we measure the transmission spectrum of the 3C-SiC modulator while launching different optical pump powers into the VGC using a pump-probe approach (see Methods). Note that the coupling loss of each VGC is around 10 dB for the transverse electric (TE) polarized light used here. The results are displayed in Fig. 4a, showing a redshift of the resonance, where the magnitude of the shift increases linearly with pump power, indicating the expected optothermal effect, which can be minimized via temperature stabilization or cladding optimization^{37,38}. The degradation of the optical Q is

negligible, even if the input optical power is increased to 500 mW. Moreover, to measure the relaxation of the optical microcavity, we measure the time-dependent change of the resonance by switching off the 500 mW optical pump (see Methods). Figure 4b shows the resonance wavelength relaxes according to a single exponential function. The exponential decay owes to a resonance shift from the cool-down process after the pump power is off³⁹, corroborating the redshift of the spectrum observed earlier, further indicating its thermal origin.

To quantify operation at high and continuous optical intensities, we measure the EO response of the modulator with varied optical input power. The results are shown in Fig. 5a, in

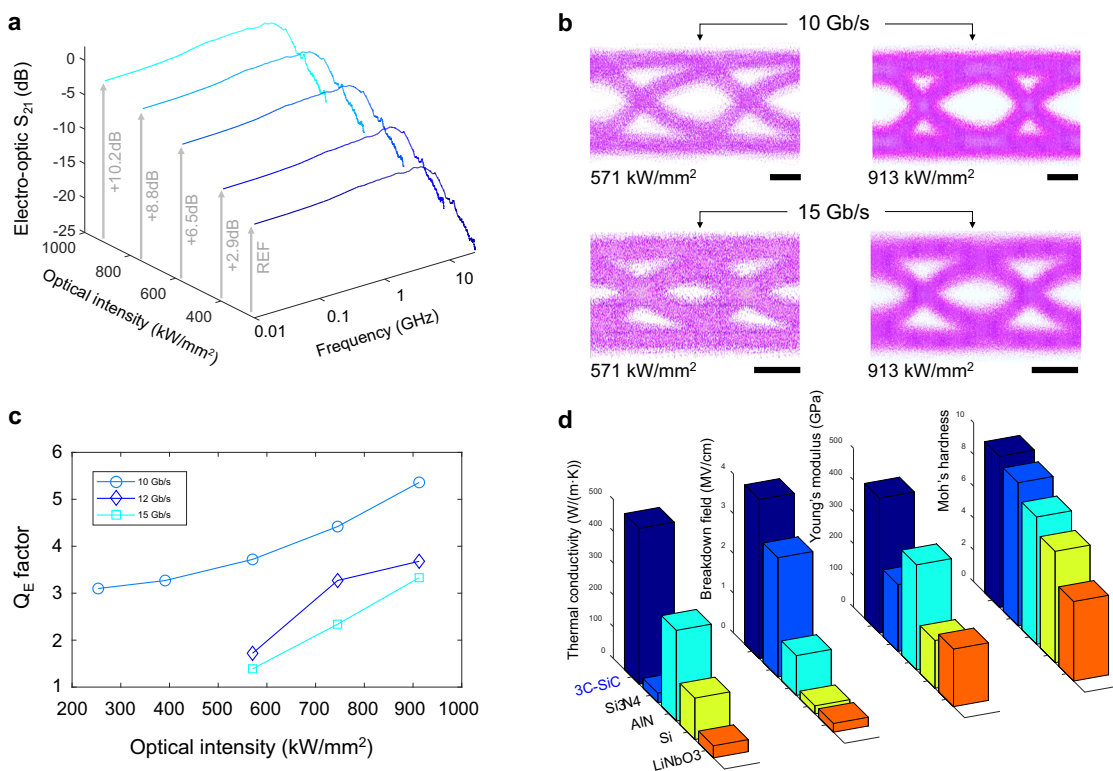


Fig. 5 High-power operation and material comparison. **a** Electro-optic s_{21} parameter characterization at high optical intensities shows an improvement in RF responses. **b** Measured eye diagrams at 10 Gb/s and 15 Gb/s. The high-bandwidth photodiode is directly connected to a real-time oscilloscope for recording eye diagrams without equalization. No low-pass RF filter is used in the measurement. Measured eye diagrams confirm increased eye opening and no signal degradation when operating the modulator at high optical intensities. **c** Q_E factors as a function of optical intensity for bit rates of 10 Gb/s, 12 Gb/s, and 15 Gb/s show an improved and robust modulation performance for higher input intensity. The high-bandwidth photodiode is directly connected to a real-time oscilloscope for recording eye Q_E factors without equalization. No low-pass RF filter is used in the measurement. **d** Material parameter comparison of 3C-SiC with widely used optical materials showing the distinct advantages of SiC for high power handling. Scale bars, 33 picoseconds.

which the optical intensity within the waveguide at the resonance wavelength is calculated from the peak circulating power within the ring resonator⁴⁰. It shows, by increasing the optical intensity from 254 kW/mm² to 913 kW/mm² (corresponding to optical input powers from 6.8 mW to 24.5 mW, respectively), and after accounting for optical insertion loss, the EO response is enhanced by up to 10.2 dB. We observe this without evidence of signal distortion or saturation of modulation efficiency, with the limiting factor being the fiber damage threshold. The observed eye diagrams (Fig. 5b) also exhibit enlarged openings at 10 Gb/s and 15 Gb/s with increased optical intensities. This is due to the increase in signal-to-noise ratio at a higher optical power, which consequently improves the ability to transmit data at a higher speed. High-power operation thus shows improved modulation performance for digital signals and the ability to reach larger bandwidths. Moreover, Fig. 5c shows at an optical intensity of 913 kW/mm² and without equalization and low-pass filtering, $Q_E > 2.7$ for all data rates at $V_{pp} = 2$ V. This confirms the operation of the modulator at high optical intensities.

To distinguish SiC for optical and electrical integration, we compare the material parameters of several EO modulator platforms (Fig. 5d). The large thermal conductivity of 3C-SiC (490 W/(m·K)), which is almost double that of AlN⁴¹ and more than 12-fold larger than LiNbO₃⁴² benefits SiC for high-power EO applications and co-integration with electronics. Furthermore, the ultra-high breakdown field of 3C-SiC (4 MV/cm), which is 18-fold higher than LiNbO₃, enables the possibility to integrate RF amplifiers on chip with the modulator as well as making it resistant to electro-magnetic attacks from RF bursts.

Moreover, the high radiation hardness, together with the high Moh's hardness and large Young's modulus of SiC also present advantages in harsh operating environments⁴.

Discussion

We demonstrate an integrated Pockels modulator in SiC with a CMOS compatible drive voltage, small device footprint, and continuous low-noise data modulation at high optical intensities. We envision a future device that could achieve improved linearity, spur-free dynamic range, and frequency response by implementing a SiC Mach-Zehnder modulator. Our SiC EO modulator opens opportunities for direct SiC optoelectronic integration using CMOS foundries with the benefit to various applications ranging from optical networks, chip-scale interconnects, RF and microwave photonics, and quantum photonics. Our work constitutes an essential component of an envisioned thin-film SiC platform consisting of monolithic integration of modulators, photodiodes, frequency converters, and quantum functionalities for on-chip photonics. Finally, the ability to integrate with electronics could inspire a generation of integrated devices for photonic signal processing, chip-to-chip, or intra-chip interconnects, thereby ushering in an era of scalable optoelectronics.

Methods

Device fabrication. Devices are fabricated from a commercially available 3C-SiC on a silicon wafer with 3.5 μm of SiC epitaxially grown on a silicon substrate supplied by NOVAsiC. A 2 μm-thick low pressure chemical vapor deposition (LPCVD) SiO₂ is deposited onto the SiC thin film, and the resultant stack is Van der Waals bonded to a thermal SiO₂ on silicon wafer before thinning down SiC via

an inductively coupled plasma reactive ion etching (ICP-RIE) process. The device consists of a thin 3C-SiC layer, LPCVD SiO₂, and a silicon substrate for the handle. The waveguides and grating couplers are patterned on 2 μm of hydrogen silsesquioxane (FOX-16) resist using EBL. They are subsequently etched into the SiC layer using an ICP-RIE process consisting of the CMOS foundry compatible gases SF₆ and C₄F₈⁷. The built-up polymer due to C₄F₈ etch gas is removed using a two-step wet cleaning process. First, a solution of hydrogen peroxide and ammonium hydroxide is used to remove the polymer. Second, a solution of hydrogen peroxide and hydrochloric acid is used to remove the metal ions from the surface of the etched waveguides. Plasma enhanced chemical vapor deposition (PECVD) process is used to deposit a 1 μm layer of SiO₂ onto the fabricated devices to act as an insulation layer between the electrodes and the device, which is sufficiently thick to minimize excess absorption due to the metal electrodes. Device electrodes fabrication involves EBL patterning on Polymethyl methacrylate resist, developed with a mixed solution of one part Methyl isobutyl ketone and three parts Isopropyl alcohol. Metal layers consisting of 5 nm titanium and 500 nm of gold are deposited using electron beam evaporation followed by lift-off using a solution of N-Methyl-2-pyrrolidone.

Electro-optic characterization and transmission spectrum measurement. Laser light (Keysight 81960 A) around 1550 nm is amplified using an Amonics erbium-doped fiber amplifier (EDFA) followed by an optical bandpass filter to reduce amplified spontaneous emission noise. The resultant light is launched into the ring modulator (Supplementary Fig. 1a). The laser is tuned to a wavelength that matches the most linear edge of a resonance to ensure minimal distortion in the modulated signal. A second EDFA is placed after the modulator to compensate for optical loss before the optical to electrical conversion via a 20 GHz photodetector (Discovery). A high-speed microwave probe (GGB) is used to deliver the modulation signal to the input port of the transmission line. To measure the EO response, the sinusoidal signal with sweeping frequency from a signal generator of a vector network analyzer (VNA, Keysight N5234A) is used to drive the modulator via the microwave probe, while the photodetector output is connected to the VNA receiver. EO response is obtained from the s-parameter of the VNA, where RF cable losses are calibrated out of the measured frequency responses. To measure the high-speed data modulation, electrical PRBS signals of voltage varied from 0.2 V_{pp} to 2 V_{pp} are generated from a 65 GSa/s arbitrary waveform generator (AWG, Keysight M8195A) and then connected with the microwave probe (Supplementary Fig. 1b). A real-time digital sampling oscilloscope with an analog bandwidth of 110 GHz (Keysight UXR series) is used to capture the received signal from the photodetector. The oscilloscope acts as the receiver for the PRBS, where a second-order phase-locked loop is used for clock recovery to generate an eye diagram of the received data. The eye Q_E factor was measured directly from the oscilloscope using persistence mode for a fixed number of waveforms.

The BER^{30,31} is obtained from the eye Q_E factor measured by using a low-pass RF filter (MiniCircuits VLF-6400+) at the output of the photodetector to reduce inter-symbol interference. The signal from the output of the low-pass RF filter is captured by a real-time digital sampling oscilloscope with an analog bandwidth of 70 GHz (Tektronix DPO77002SX). Eye diagrams and Q_E are measured via the oscilloscope without equalization.

By scanning the wavelength of the tunable laser and detecting the optical power (Keysight N7744A) at the optical output of the modulator, the transmission spectra for different DC voltages are obtained. DC bias voltages from -20 V to +20 V are applied on the modulator ground-signal-ground electrodes and the transmission spectra graphed (Supplementary Fig. 2).

Pockels coefficient extraction. Finite element method solver (COMSOL Multiphysics) is used to simulate the optical mode profile and the electric field distribution inside the SiC waveguide. The electro-optic overlap integral^{24,25} (Γ) is numerically calculated to be 0.184 to evaluate the interaction of optical and electric fields based on the measured waveguide and electrode geometries shown in Fig. 1c. The effective refractive index (*n*_{eff}) of the fundamental TE mode within the SiC on insulator waveguide at the operating wavelength is 2.27. The modulation index is determined using the Jacobi-Anger expansion method which is obtained from the optical power ratio of the modulated sideband and the optical carrier. The voltage-induced effective refractive index change of the fundamental TE mode is calculated to be $1.37 \times 10^{-6}/V$ from the measured resonance shift, and then the EO coefficient (*r*) of the 3C-SiC waveguide at the operating wavelength is derived correspondingly⁴³. Considering the refractive index (*n*) of SiC is 2.57²⁹ and the electrode gap (*g*) is 1.9 μm in the experiment, the half-wave voltage-length product (*V*_π*L*) at the operating wavelength (*λ*₀) of 1544 nm is calculated to be ~55 V-cm, where $V_{\pi}L = n_{\text{eff}}\lambda_0 g / (n^2 r)$.

Pump-probe measurement. Frequency domain analysis: Light (pump) from a tunable laser (Keysight 81950 A) is amplified by an EDFA to increase the optical power and then coupled into the 3C-SiC modulator placed on a heat sink, where the pump is aligned to the optical resonance of the modulator (1544 nm wavelength). A low-power probe beam, which is synchronized with an optical spectrum analyzer (AP2083A), is used to monitor the transmission spectrum using a resonance that is about ten FSRs red-detuned from the pump (Supplementary Fig. 3). The probe power that is launched into the modulator has a power of <10 μW such

that it introduces negligible nonlinear optical effects. Time-domain analysis: We use an optical switch (rise time 1 μs) to switch off the 500 mW power pump beam while keeping the probe beam on. We observe a shift of the cavity resonance at the probe wavelength that follows an exponential dependence owing to the cooling of the resonator. The probe light is tuned to the side of fringe of the optical resonance so that the resonance wavelength change results in the variation of optical power detected by a photodetector connected to an oscilloscope.

Material parameter comparison. Supplementary Table 1 lists the comparison of common photonic integration materials with 3C-SiC, specifically parameters related to power handling of the modulator. The Young's modulus and Moh's hardness are useful parameters for a broad range of applications. Moreover, the refractive index and electrical permittivity are also listed. Low electrical permittivity combined with a higher refractive index is favorable for a larger modulation efficiency at a given EO coefficient.

Data availability

Supplementary Information is available in the online version of the paper. Source data are provided with this paper and also available on Zenodo: <https://zenodo.org/record/6342493>.

Received: 17 June 2021; Accepted: 11 March 2022;

Published online: 05 April 2022

References

- Nakamura, D. et al. Ultrahigh-quality silicon carbide single crystals. *Nature* **430**, 1009–1012 (2004).
- Lukin, D. M. et al. 4H-silicon-carbide-on-insulator for integrated quantum and nonlinear photonics. *Nat. Photonics* **14**, 330–334 (2020).
- Atatüre, M., Englund, D., Vamivakas, N., Lee, S. Y. & Wrachtrup, J. Material platforms for spin-based photonic quantum technologies. *Nat. Rev. Mater.* **3**, 38–51 (2018).
- Lee, T. H., Bhunia, S. & Mehregany, M. Electromechanical computing at 500 °C with silicon carbide. *Science* **329**, 1316–1318 (2010).
- Anderson, C. P. et al. Electrical and optical control of single spins integrated in scalable semiconductor devices. *Science* **366**, 1225–1230 (2019).
- Ghelfi, P. et al. A fully photonics-based coherent radar system. *Nature* **507**, 341–346 (2014).
- Powell, K. et al. High-Q suspended optical resonators in 3C silicon carbide obtained by thermal annealing. *Opt. Express* **28**, 4938–4949 (2020).
- Choi, S. R., Kim, D., Choa, S. H., Lee, S. H. & Kim, J. K. Thermal conductivity of AlN and SiC thin films. *Int. J. Thermophys.* **27**, 896–905 (2006).
- Nabki, F., Dusatko, T. A., Vengallatore, S. & El-Gamal, M. N. Low-stress CMOS-compatible silicon carbide surface-micromachining technology-part I: process development and characterization. *J. Microelectromech. Syst.* **20**, 720–729 (2011).
- Boyd, R. W. *Nonlinear Optics*. (Academic, 2003).
- Li, M. & Tang, H. X. Strong Pockels materials. *Nat. Mater.* **18**, 9–11 (2019).
- Tang, X., Irvine, K. G., Zhang, D. & Spencer, M. G. Linear electro-optic effect in cubic silicon carbide. *Appl. Phys. Lett.* **59**, 1938–1939 (1991).
- Barrios, C. A., Thomas, C. I., Spencer, M. & Lipson, M. 3C-SiC modulator for high-speed integrated photonics. *Mater. Res. Soc. Symp. - Proc.* **799**, 223–227 (2003).
- Vonsovici, A., Reed, G. T. & Evans, A. G. R. β-SiC-on insulator waveguide structures for modulators and sensor systems. *Mater. Sci. Semicond. Process.* **3**, 367–374 (2000).
- Liu, Y. M. & Prucnal, P. R. Low-loss silicon carbide optical waveguides for silicon-based optoelectronic devices. *IEEE Photonics Technol. Lett.* **5**, 704–707 (1993).
- Reed, G. T. et al. Fabrication and evaluation of SiC optical modulators. *Symp. Integr. Optoelectronic Devices* **4654**, 145–156 (2002).
- Cardenas, J. et al. High Q SiC microresonators. *Opt. Express* **21**, 16882–16887 (2013).
- Lu, X., Lee, J. Y., Feng, P. X.-L. & Lin, Q. High Q silicon carbide microdisk resonator. *Appl. Phys. Lett.* **104**, 181103 (2014).
- Fan, T., Moradinejad, H., Wu, X., Eftekhari, A. A. & Adibi, A. High-Q integrated photonic microresonators on 3C-SiC-on-insulator (SiCOI) platform. *Opt. Express* **26**, 25814–25826 (2018).
- Lukin, D. M., Guidry, M. A. & Vučković, J. Integrated quantum photonics with silicon carbide: challenges and prospects. *PRX Quantum* **1**, 020102 (2020).
- Marpaung, D., Yao, J. & Capmany, J. Integrated microwave photonics. *Nature* **13**, 80–90 (2019).

22. Holzgrafe, J. et al. Cavity electro-optics in thin-film lithium niobate for efficient microwave-to-optical transduction. *Optica* **7**, 1714–1720 (2020).
23. Yu, H. et al. Trade-off between optical modulation amplitude and modulation bandwidth of silicon micro-ring modulators. *Opt. Express* **22**, 15178–15189 (2014).
24. Boynton, N. et al. A heterogeneously integrated silicon photonic/lithium niobate travelling wave electro-optic modulator. *Opt. Express* **28**, 1868–1884 (2020).
25. Xiong, C., Pernice, W. H. P. & Tang, H. X. Low-loss, silicon integrated, aluminum nitride photonic circuits and their use for electro-optic signal processing. *Nano Lett.* **12**, 3562–3568 (2012).
26. Berseth, C. A., Wuethrich, C. & Reinhart, F. K. The electro-optic coefficients of GaAs: measurements at 1.32 and 1.52 μm and study of their dispersion between 0.9 and 10 μm . *J. Appl. Phys.* **71**, 2821–2825 (1992).
27. Suzuki, N. & Tada, K. Electrooptic properties and Raman scattering in INP. *Jpn. J. Appl. Phys.* **23**, 291–295 (1984).
28. Patrick, L. & Choyke, W. J. Static dielectric constant of SiC. *Phys. Rev. B* **2**, 2255–2256 (1970).
29. Tropf, W. J., Thomas, M. E. & Linevsky, M. J. Infrared refractive indices and thermo-optic coefficients for several materials. *Johns Hopkins APL Tech. Dig.* **3425**, 160–171 (1998).
30. Freude, W. et al. Quality metrics for optical signals: eye diagram, Q-factor, OSNR, EVM and BER. In *Proc. 14th International Conference on Transparent Optical Networks* 1–4 (IEEE, Coventry, 2012).
31. Muehlbrandt, S. et al. Silicon-plasmonic internal-photoemission detector for 40 Gbit/s data reception. *Optica* **3**, 741–747 (2016).
32. Cho, J., Xie, C. & Winzer, P. J. Analysis of soft-decision FEC on non-AWGN channels. *Opt. Express* **20**, 7915–7928 (2012).
33. Asif, R. Advanced and flexible multi-carrier receiver architecture for high-count multi-core fiber based space division multiplexed applications. *Sci. Rep.* **6**, 27465 (2016).
34. Jiang, H. et al. Fast response of photorefraction in lithium niobate microresonators. *Opt. Lett.* **42**, 3267–3270 (2017).
35. Kosma, K., Konidakis, I. & Pissadakis, S. Photorefractive tuning of whispering gallery modes of a spherical resonator integrated inside a microstructured optical fibre. *Eur. Phys. J. Spec. Top.* **223**, 2035–2040 (2014).
36. Savchenkov, A. A., Matsko, A. B., Strekalov, D., Ilchenko, V. S. & Maleki, L. Enhancement of photorefraction in whispering gallery mode resonators. *Phys. Rev. B* **74**, 245119 (2006).
37. Kim, M. et al. Silicon electronic–photonic integrated 25 Gb/s ring modulator transmitter with a built-in temperature controller. *Photon. Res.* **9**, 507–513 (2021).
38. Ling, J. et al. Athermal lithium niobate microresonator. *Opt. Express* **28**, 21682–21691 (2020).
39. Chen, W., Zhu, J., Özdemir, S. K., Peng, B. & Yang, L. A simple method for characterizing and engineering thermal relaxation of an optical microcavity. *Appl. Phys. Lett.* **109**, 061103 (2016).
40. Ikeda, K., Saperstein, R. E., Alic, N. & Fainman, Y. Thermal and Kerr nonlinear properties of plasma-deposited silicon nitride/ silicon dioxide waveguides. *Opt. Express* **16**, 12987–12994 (2008).
41. Zhu, S. & Lo, G.-Q. Aluminum nitride electro-optic phase shifter for backend integration on silicon. *Opt. Express* **24**, 12501–12506 (2016).
42. Arizmendi, L. Photonic applications of lithium niobate crystals. *Phys. Status Solidi A* **201**, 253–283 (2004).
43. Honardoost, A., Safian, R., Rao, A. & Fathpour, S. High-speed modeling of ultracompact electrooptic modulators. *J. Light. Technol.* **36**, 5893–5902 (2018).

Acknowledgements

We thank S. Desai for discussions on device simulation, C. Lu for discussions on modulator testing, C. Yu for feedback on the manuscript. Device fabrication and characterization were carried out in part at the Harvard University Center for Nanoscale Systems (CNS), a member of the National Technology Coordinated Infrastructure Network, and the University of Sydney. This work was supported by the Sydney Research Accelerator Fellowship and Harvard University Mobility Scheme. J. W. and D. M. acknowledge the support of Research Training Program Scholarships from the University of Sydney. N. S. acknowledges the support of the Natural Sciences and Engineering Research Council of Canada (NSERC), and NSF STC “Center for Integrated Quantum Materials” under Cooperative Agreement No. DMR-1231319. M. L. acknowledges support from the Airforce Office of Scientific Research (AFOSR) under grant FA9550-19-1-0376.

Author contributions

K. P., M. L., and X. Y. conceived the experiment. K. P., L. L., A. S. -A., and J. D. fabricated the devices. J. W. and D. M. performed numerical simulations. K. P., L. L., J. D., and N. S. carried out the device characterization. K. P., N.S., and X. Y. wrote the manuscript with contributions from all authors. M. L. and X. Y. supervised the project.

Competing interests

The authors declare no competing interests.

Additional information

Supplementary information The online version contains supplementary material available at <https://doi.org/10.1038/s41467-022-29448-5>.

Correspondence and requests for materials should be addressed to Marko Lončar or Xiaoke Yi.

Peer review information *Nature Communications* thanks Michael (G.) Spencer and the other, anonymous, reviewer(s) for their contribution to the peer review of this work.

Reprints and permission information is available at <http://www.nature.com/reprints>

Publisher's note Springer Nature remains neutral with regard to jurisdictional claims in published maps and institutional affiliations.



Open Access This article is licensed under a Creative Commons Attribution 4.0 International License, which permits use, sharing, adaptation, distribution and reproduction in any medium or format, as long as you give appropriate credit to the original author(s) and the source, provide a link to the Creative Commons license, and indicate if changes were made. The images or other third party material in this article are included in the article's Creative Commons license, unless indicated otherwise in a credit line to the material. If material is not included in the article's Creative Commons license and your intended use is not permitted by statutory regulation or exceeds the permitted use, you will need to obtain permission directly from the copyright holder. To view a copy of this license, visit <http://creativecommons.org/licenses/by/4.0/>.

© The Author(s) 2022